Nanoscale

Accepted Manuscript

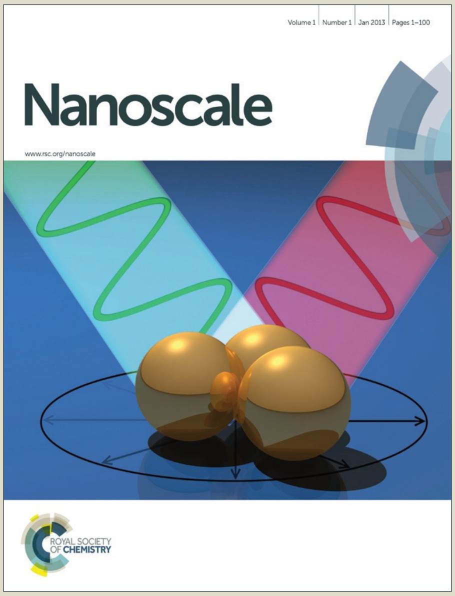

ROYAL SOCIETY OF CHEMISTRY

www.rsc.org/nanoscale

Journal Name

ARTICLE

Bottom-up Synthesis of High-performance Nitrogen-enriched Transition Metal/ Graphene Oxygen Reduction Electrocatalysts both in Alkaline and Acid Solution

Received 00th January 20xx,
Accepted 00th January 20xx

DOI: 10.1039/x0xx00000x

www.rsc.org/

Qingxue Lai,[a] Qingwen Gao,[a] Qi Su,[a] Yanyu Liang,*[a] Yuxi Wang,[b] and Zhi Yang*[b]

Oxygen reduction electrocatalysts with low-cost and excellent performance have been urgently required for large-scale application of fuel cells and metal–air batteries. Though nitrogen-enriched transition metal/graphene hybrids (N-TM/G, TM=Fe, Co, and Ni and related compounds) have been developed as novel substitutes for precious metal catalysts (PMCs) towards oxygen reduction reaction (ORR), a significant challenge still remains for simple and efficient synthesis of N-TM/G catalysts with satisfactory electrocatalytic behaviors. Herein, we demonstrate a universal bottom-up strategy for efficient fabrication of strong-coupled N-TM/G catalysts. This strategy is implemented via direct polymerization of transition metal phthalocyanine (TMPc) in two-dimensional confined space of in situ generated g-C_3N_4 and subsequent pyrolysis. Such a space-confined bottom-up synthesis route successfully constructs a strong-coupled triple junction of transition metal-graphitic carbon-nitrogen-doped graphene (TM-GC-NG) with extensive controllability over specific surface area, nitrogen content/types as well as the states of metal. As a result, the optimized N-Fe/G materials show a promising potential as high-performance NPMCs towards ORR both in alkaline and acid solution.

Introduction

Electrochemical energy devices, such as fuel cells, metal-air batteries, Li-ion batteries and supercapacitors, have been recognized as the most promising alternative sustainable energy technologies for portable, stationary, and transportation applications.[1-5] For both fuel cells and metal–air batteries, the performance characteristics of these electrochemical energy devices are greatly depended on the sluggish oxygen reduction reaction (ORR), which calls for effective oxygen reduction electrocatalysts for their widespread application.[6,7] Even though conventional Pt-based ORR catalysts have been the state of the art for oxygen reduction in different conditions, their disadvantages of high cost, limited stability and fast deactivation make it hardly to meet the needs of practical application.[8] Cheap nanocarbon materials with excellent electronic and surface properties have played a critical role in the field of energy storage and conversion[9-12] and are thus considered as one kind of the most promising alternative non-precious metal catalysts (NPMCs) towards ORR.[13-16]

Recent theoretical calculation and experiment results have demonstrated that nitrogen doping-based activation of the π electrons of carbon matrix coupled with enhanced synergy effect among multiple active sites trapped on a special nanostructure creates novel and promising nitrogen-rich transition metal/nanocarbon (N-TM/C) systems.[17-21] Among them, graphene-based N-TM/C catalysts (N-TM/G) have drawn more attention due to their unique two-dimensional nanostructure-dependent properties.[22-24] It should be noted that ORR in different environments (for example, acid or alkaline conditions) perhaps undergo different reaction mechanisms, which calls for rational design and controllable build of suitable catalytic sites for the corresponding condition. Even though the active sites in N-TM/G catalysts have not been clearly understood, pydinic- and graphitic-typed nitrogen sites in nanocarbon matrix and transition metal–related compounds (for example, metallic Fe and Co; Fe_3C, FeN, CoO and Co_3O_4) have been generally considered as effective active sites for catalysis of oxygen reduction to hydroxyl (OH^-) in alkaline solution. On the contrary, instead of the above active sites, a type of Fe (or Co)-N_x coordination centre in nanocarbon matrix is urgently desired for catalysis of oxygen reduction to water in acid solution. Hence, effective nitrogen-doped sites, stable and active transition metal-related compounds as well as Fe (or Co)-N_x coordination centres are all necessary for N-TM/G to achieve excellent catalytic performance in the both conditions. Besides the composition, strongly coupled TM-G interfacial structures with highly opened channels are also a prerequisite to the marked

---

[a] College of Material Science and Technology, Nanjing University of Aeronautics and Astronautics, Yudao St. 29, 210016, Nanjing, P. R. China
[b] Key Laboratory for Thin Film and Microfabrication of Ministry of Education,, Shanghai Jiao Tong University, Dongchuan Road 800, 200240, Shanghai, P. R. China
[c] Corresponding author: E-mail: liangyy403@126.com (Y. Y. Liang) and zhiyang@sjtu.edu.cn (Z. Yang)

† Electronic Supplementary Information (ESI) available: [details of experiment process, physical characterization and additional data are available]. See DOI: 10.1039/x0xx00000x

improvement of catalysts' activity, selectivity and stability.[25,26] To meet the special requirements for the composition, nanostructure as well as low processing cost demands precise controllable synthesis of N-TM/G via a simple and feasible route.

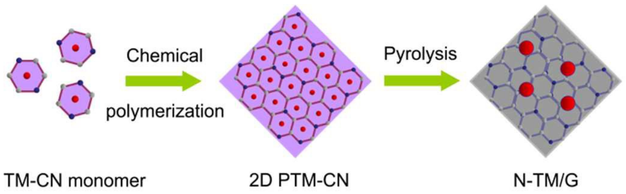

Scheme 1. Theoretical synthesis process of N-TM/G hybrids by bottom-up method.

Conventional synthesis route of N-TM/G is graphene oxide (GO)-based soft chemistry method usually combined with controllable pyrolysis technologies,[27,28] which demands multiple-step synthesis route with precise regulation requirements as well as unavailable costs, greatly limiting the large-scale manufacture of these N-TM/G materials. Recently the significant breakthroughs in the synthesis strategy of nanocarbon-based materials, especially the development of g-C_3N_4-based self-sacrificed route[29] and salt-templating method[30-32], make it more possible for facile synthesis of N-TM/G catalysts. Herein we propose a versatile bottom-up protocol towards controllable synthesis of N-TM/G catalysts. As shown in Scheme 1, N-TM/G catalysts can be conveniently synthesized by choosing a polymerizable monomer containing TM, C and N (TM-CN) and controlling its polymerization and carbonization reaction to create a 2D graphene nanosheet-based structure via a simple path. Importantly, instead of anchoring TM to NG surface in conventional methods, TM here is migrated from the carbon matrix to its surface, which could create a strong-coupled TM-NG interface for ORR. In order to confirm the feasibility of this strategy, transition metal-phthalocyanines compounds (TMPcs, TM=Fe, Co and Ni) are chose as the beginning block unit and melamine-derived g-C_3N_4 as the 2D structure guiding agent to synthesize N-TM/G hybrids. The resulted N-TM/G catalysts have a high activity, excellent four-electron selectivity as well as strong stability and tolerance to methanol both in alkaline and acid solution.

Results and discussion

Characterization of the Structure and Composition of the Controllable Synthesized N-TM/G catalysts

The synthesis process of N-TM/G catalysts was direct pyrolysis of the mixture of melamine and TMPc under N_2 atmosphere at high temperature (See details in supporting information). The products are donated as N-TM/G (W)-T (W= the addition [mg] of TMPc vs. a fixed addition of melamine (4.00 g), T= target temperature) and N-TM/G (W)-T-S (S= acid treatment and second heat treatment). As shown in Figure 1 a, the obtained sample is spongy continuous monolith with an excellent lightweight property. The powder X-ray diffraction (XRD) patterns of N-TM/G (60)-900 in Figure 1 b confirm that graphitic carbon phase with a typical C (002) diffraction peak at around 26.1^{o} is formed in these hybrids. On the other hand, metallic Co (PDF#15-0806) and Ni (PDF#87-0712) are generated in N-Co/G (60)-900 and N-Ni/G (60)-900, respectively, while metal carbide Fe_3C (PDF#85-1317) and metallic α-Fe (PDF#87-0722) phases are formed in N-Fe/G (60)-900.[33] The metal loading characterized by thermogravimetric differential scanning calorimetry (TG-DSC) analysis is 21.44 wt.%, 23.55 wt.% and 25.26 wt.% for N-Fe/G (60)-900, N-Co/G (60)-900 and N-Ni/G (60)-900, respectively (Figure S1). The special composition of these materials promises them a certain magnetic property (Figure S2), especially for N-Fe/G (60)-900 (15.9 emu/g) and N-Co/G (60)-900 (14.2 emu/g), resulting into a potential benefit for facile recycle and regeneration by simple magnetic separation.[34]

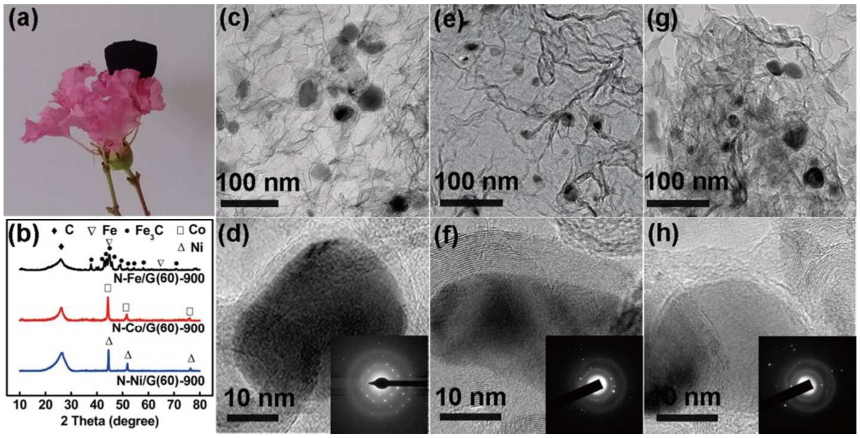

Figure 1. The composition and morphology of N-TM/G. (a) A N-Fe/G(60)-900 cylinder on a fresh flower; (b) XRD patterns of N-TM/G (60)-900; (c-h) TEM images of N-TM/G: (c, d) N-Fe/G (60)-900; (e, f) N-Co/G (60)-900; (g, h) N-Ni/G (60)-900 (inset: the corresponding SAED of metal NP).

The transmission electron microscopy (TEM) images (Figure 1 c-h) uncover that two-dimensional (2D) flexible and almost transparent N-doped graphene (NG) nanosheet with abundant crumples is formed in the three kinds of catalysts; meanwhile, metallic nanoparticles (NPs) with a narrow size range of about 5~30 nm are even-distributed on the NG surface. Notably, these metallic NPs surface is uniform encapsulated by graphitic carbon (GC) shells, in situ forming well-defined TM-GC core-shell structure. Finally strong-coupled TM-GC-NG triple junction is created by this bottom-up synchronous construction strategy.

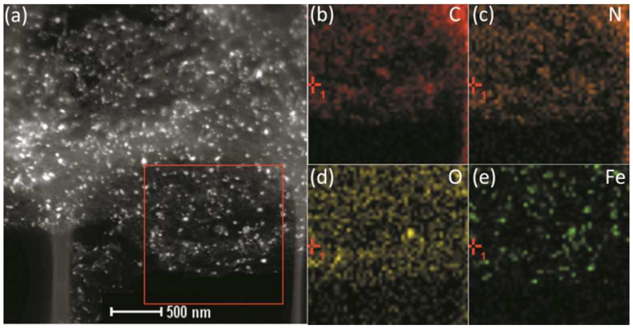

Figure 2. (a) Typical STEM image of N-Fe/G (60)-900 and corresponding element mapping images taken in the red square region in Figure 3(a): (b) C; (c) N; (d) O; (e) Fe.

Typical scanning transmission electron microscopy (STEM) image (Figure 2a) of N-Fe/G (60)-900 clearly reveals that nanoscale Fe/Fe$_3$C NPs with a uniform size were homogeneously anchored on the surface of thin and almost transparent graphene nanosheet. Figure 2b-e are mapping images of four elements (C, N, O and Fe) in N-Fe/G (60)-900 sample. It can be found that numerous nitrogen as well iron element is evenly distributed in this sample. In addition, oxygen element is observed in this sample, even though no oxygen-contained compound is introduced during the whole synthesis process, which should be ascribed to the surface-absorbed water or other oxygen-contained small molecules.[29]

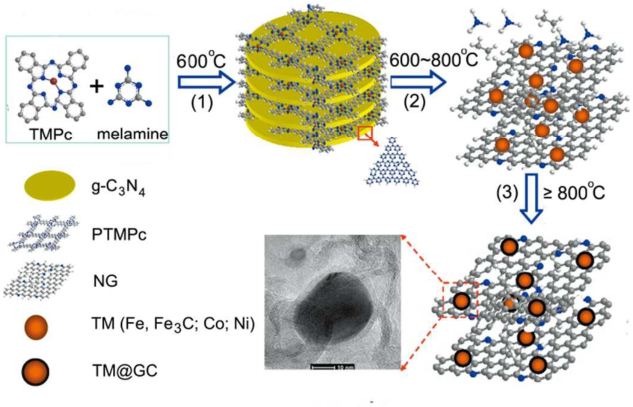

Figure 3. Proposed space-confined synthesis mechanism of N-TM/G.

The above results present well-defined 2D nanostructured N-TM/G materials. A complex TM-GC-NG triple junction structure with strong interaction is successfully built in these hybrids. It must be point out that such a unique structure is achieved via one-pot one-step route without any other post-treat. Further analysis of the intermediate products reveals that the main component is g-C$_3$N$_4$ which has a typical micrometer-scale nanosheet structure (Figure S3). XPS results (Figure S4) demonstrate that except the pydinic- and graphitic-typed nitrogen in g-C$_3$N$_4$, obvious pyrrolic-typed nitrogen is observed; meanwhile, no α-Fe or Fe$_3$C but strong signal peaks of Fe^{2+} at 708.8eV and Fe^{3+} at 711.2eV in Fe2p XPS spectra appear. Notably, no Fe-O bonds (~529.5 eV) are observed in the O1s high-resolution XPS sepctrum, suggesting that the pyrrolic Fe-N$_4$ structures are still remained at 600°C and probably exist in FePc polymer (PFePc) formed via thermal polymerization. Based on the above analysis, a space-confined synthesis mechanism is proposed to explain the formation of N-TM/G, as shown in Figure 3. The possible process is as follows: (1) Thermal polymerization of melamine and TMPc into g-C$_3$N$_4$ and PTMPc, respectively, below 600^{o}C; at the same time, PTMPc is confined into the large interlayer space of g-C$_3$N$_4$ to form 2D nanostructure. (2) During 600~800^{o}C, g-C$_3$N$_4$ is decomposed, making the 2D PTMPc separated while PTMPc begins to be pyrolyzed into amorphous carbon and metal NPs. (3) With the exposure of metal NPs, the carbon/nitrogen-enriched small molecules derived from g-C$_3$N$_4$ are facilly pyrolyzed and reconstructed on the metal surface to form GC shells with a certain amount of doped nitrogen; at the same time, a second doping of nitrogen into the whole carbon framework is achieved. Finally N-TM/G materials with strong-coupled TM-GC-NG triple junction are achieved via the bottom-up strategy.

Excitingly, such simple synthesis process can realize controllable the surface properties for the as-prepared catalysts in a wide range via simply adjusting the carbonization temperature and raw material proportion. Firstly, the degree of graphitization, an indispensable condition for efficient and stable catalysis for nanocarbon-based electrocatalysts, is obviously regulated by changing the heat treatment temperature. As shown in Figure 4a, the intensity of diffraction peaks of C (002) is strengthened with increased temperature from 800^{o}C to 1000^{o}C. Meanwhile, Raman spectra of N-Fe/G hybrids in Figure 4b show that the value of I_D/I_G is decreased from 1.05 to 0.75 during this process, an obvious evidence for enhancement of graphitic degree of C in N-Fe/G catalyst.[35] Especially, the high-resolution C1s spectra of N-Fe/G in Figure 4d can directly prove the improvement on the degree of graphitization. The bonded carbon can be decomposed mostly into four components: C=C (C1, 284.5eV), C-O/N (C2, 285.6eV), C=O (C3, 287.7eV) and O-C=O (C4, 288.5eV).[36] Remarkably, the significant difference of the sp^2-hybridized carbon atom (C1 type; 34.7 at.%, 47.3 at.%, 53.3 at.% at 800^{o}C, 900^{o}C and 1000^{o}C, respectively) obviously demonstrates the improvement of graphitic degree for obtained N-Fe/G with the increase of temperature.

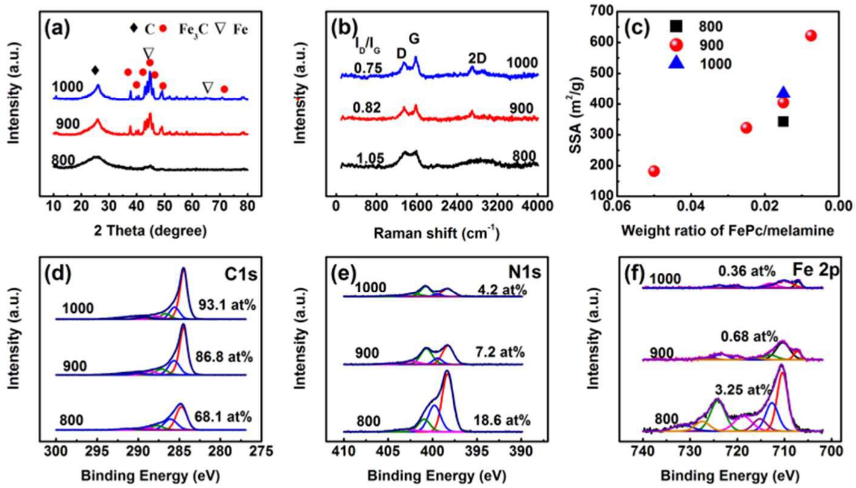

Figure 4. Physical characterization of N-Fe/G obtained at different synthesis conditions. (a) XRD patterns and (b) Raman spectra of N-Fe/G (60) with different T; (c) the dependence of SSA on the weight ratio of FePc/melamine and T; (d-f) high-resolution XPS spectra of N-Fe/G (60) with different T: (d) C1s; (e) N1s; (f) Fe2p.

Secondly, the specific surface area (SSA) of the prepared catalysts, which determining the exposure degree of active sites,[37] demonstrates a strong dependence on synthesis conditions. As shown in Figure 4c and Figure S5 and Table S1, a slow increase of product's SSA is observed with increase of the temperature. This slight change is perhaps caused by the enlargement of interbedded metal NPs which is observed by TEM images (Figure S6). It is noteworthy that a significant change of SSA is resulted from the weight ratio of FePc/melamine. It can be found that the SSA of prepared N-Fe/G hybrids can be improved from 182 m^2/g to 622 m^2/g by reducing the weight ratio from 0.05 to 0.0075. At the same time, the total pore volume of these hybrids is enhanced from 0.432 cm^3/g to 1.769 cm^3/g, with a reduction of average pore size from 19.3 nm to 16.9 nm (Table S1). The above change on SSA should be attributed to the melamine-derived g-C_3N_4 which provides a self-sacrificed 2D template for generation and decomposition of 2D TMPc polymer (PTMPc). This confinement effect can be easily enhanced via increasing the percentage of the template, resulting into much more high-opened nanochannels for full exposure of active sites.

The last and most important part is the active sites of different kinds of C-N and Fe-N bonds, which can be significantly changed by controlling the heat treatment temperature. As shown in Figure 4e, the high-resolution N1s spectrum for all samples can be deconvoluted into four peaks, corresponding to pyridinic N (N1, 398.3±0.1eV), pyrrolic N (N2, 399.5±0.1eV), graphitic N (N3, 400.8±0.1eV) and oxidized N (N4, 402.3±0.1eV).[38] The small peak shift for N2 from 800^{o}C to 900^{o}C indicates the breaking of pyrrolic N-Fe bonds in the temperature range. Furthermore, the total N content is decreased from 18.6 at.% to 4.2 at.% as the annealing temperature is increased from 800°C to 1000^{o}C. It is worthwhile to note that the pyridinic N and pyrrolic N content decreases fast (from 10.14 at.% to 1.43 at.% and 5.24 at.% to 0.32 at.%, respectively) while graphitic N content remains relatively stable (from 2.35 at.% to 1.60 at.%) during the heat treatment process. Such a change model can be attributed to the different thermodynamic stability of doped N structure. The high-resolution Fe2p spectra in Figure 4f present obvious peaks at 707.0±0.1eV, 710.3±0.1eV, 712.8±0.1eV, 719.9±0.2eV, 724.7±0.2eV and 727.6±0.2 eV, assigned to $Fe^0$2p3/2, Fe^{2+}2p3/2, Fe^{3+}2p3/2, $Fe^0$2p1/2, Fe^{2+}2p1/2 and Fe^{3+}2p3/2, respectively. The content of Fe^{3+} ions is fast decreased and Fe^0 appears when the heat treatment temperature is above 900^{o}C due to the enhanced reduction ability of carbon. As shown in (Figure S7), Mössbauer spectroscopy of N-Fe/G (60)-900 proves that most Fe atoms exist in Fe or Fe_3C and the rest Fe^{2+} ions are bonded to nitrogen atoms to form Fe^{II}-N_4/C sites, which serve as highly active catalytic sites for ORR.[39] It can be found that the surface Fe content is decreased with increasing temperature, which should be attributed to further broken of Fe-N bonds and transformation into GC encapsulated Fe/Fe_3C NPs.

Electrocatalytic Performance of the Prepared N-TM/G Catalysts both in Alkaline and Acid Solution

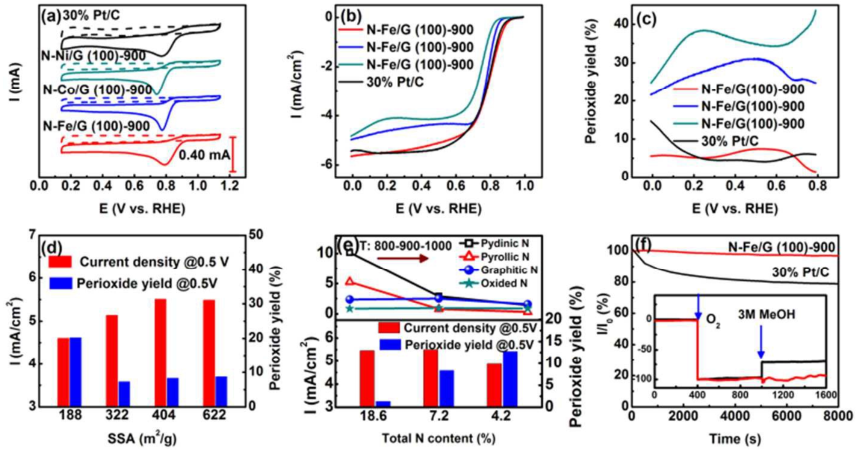

Figure 5. ORR catalytic performance of N-TM/G in 0.1 M KOH solution. (a) CV (50 mV/s; solid line: in O_2; dash line: in N_2), (b) LSV (10 mV/s with 1600rpm) and (c) HO_2^- yield of (1) N-Fe/G (100)-900, (2) N-Co/G (100)-900, (3) N-Ni/G (100)-900, and (4) 30% Pt/C catalysts in 0.1M KOH solution; (d, e) the dependence of catalytic current density and HO_2^- yield at 0.49 V vs. RHE for N-Fe/G catalysts on SSA (d) and total N content (e); (f) current-time (I-t) responses of N-Fe/NG (60)-900 and 30% Pt/C at 0.49 V vs. RHE with a rotation rate of 1600 rpm. (Catalyst loading: ~ 50 μg/cm^2 for all catalysts)

The electrocatalytic activity of prepared N-TM/G hybrids towards ORR was first estimated by cyclic voltammetry (CV) in 0.1 M KOH solution. As shown in Figure 5a, obvious cathodic peak at 0.794 V, 0.774 V, 0.743 V vs. RHE (vs. 0.782 V for 30% Pt/C) is observed for N-Fe/G (100)-900, N-Co/G (100)-900 and N-Ni/G (100)-900, respectively in O_2-saturated solution while no evident peak appears in N_2-saturated solution, demonstrating a remarkable catalytic activity towards oxygen reduction for the prepared N-TM/G catalysts. RDE voltammograms in Figure 5b show an ORR onset potential of 0.892 V, 0.847 V and 0.820 V and a catalytic current density of 5.28, 4.43 and 4.15 mA/cm^2 at 0.4 V vs. RHE for N-Fe/G (100)-900, N-Co/G (100)-900 and N-Ni/G (100)-900, respectively, compared with 0.879 V and 5.45 mA/cm^2 of commercial 30% Pt/C. These results suggest that prepared N-Fe/G has a comparable ORR activity to that of commercial 30% Pt/C while N-Co/G and N-Ni/G catalysts have a relatively low but significant activity in alkaline solution.

Meanwhile, rotating ring-disk electrode (RRDE) measurements were further revealed the ORR kinetics on prepared N-TM/G catalysts. As shown in Figure 5c and Figure S8, a low HO_2^- yield of below 7.4% at the range of 0.8V to 0 V vs. RHE is observed on N-Fe/G (100)-900 with an electron transfer number of about 3.85 at 0.50 V vs. RHE, which is very close to that of commercial 30% Pt/C, while N-Co/G (100)-900 and N-Ni/G (100)-900 catalysts generate a large amount of HO_2^- of 21%~31% and 25%~38% at that voltage range, respectively, corresponding to an electron transfer number of about 3.38 and 3.30. The above results indicate that N-Fe/G (100)-900 can catalyse oxygen directly to hydroxide with a four-electron path, resulting into better electrocatalytic selectivity towards ORR than that of N-Co/G (100)-900 and N-Ni/G (100)-900.

Systematic electrochemical tests indicate that the catalytic activity and selectivity for the prepared N-Fe/G-900 can be improved via increase the exposure degree of active sites until the maximum exposure of these active sites to the gas (O_2)-liquid (KOH solution)-solid (catalyst) interfaces when the SSA exceeds to 404 m^2/g (Figure 5d and S9). On the other hand, the catalytic selectivity of prepared N-Fe/G (60) is decreased by several times with the decrease of nitrogen content while the catalytic current keeps relatively stable until the nitrogen content is lower than 7.5 at% at a temperature higher than 900^{o}C (Figure 5e and S10). It can be concluded that pydinic and pyrrolic N in carbon matrix can strengthen the four electron selectivity while graphitic-type N is more responsible for the high catalytic current. Besides the activity and selectivity, the prepared N-TM/G catalysts also have a better stability as well as methanol-resistance ability than that of commercial 30% Pt/C catalyst. As shown in Figure 5f, as high as 97.1% of catalytic current can be maintained for N-Fe/G (60)-900 after 8000s I-t test in O_2-saturated 0.1 M KOH solution (vs. 78.8% for 30% Pt/C), and no obvious decrease of catalytic current appears on N-Fe/G (60)-900 after 3M methanol is introduced into above solution.

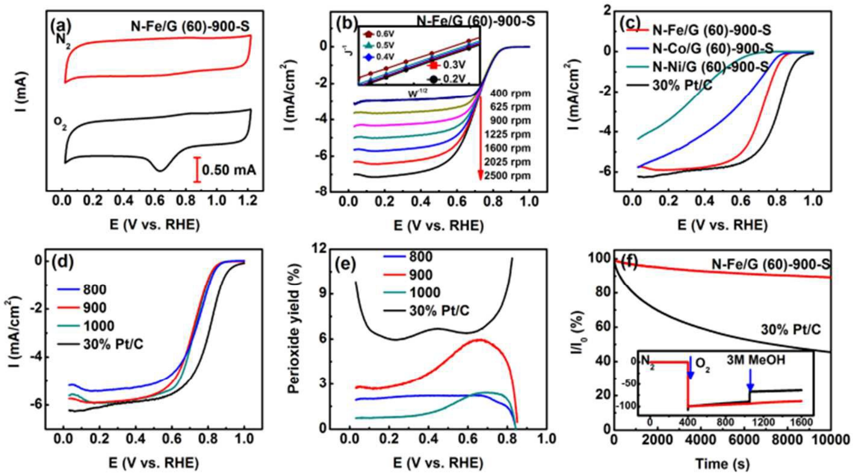

Figure 6. ORR catalytic performance of N-TM/G-S in 0.1 M $HClO_4$ solution. (a) CV and (b) LSV curves of N-Fe/G(60)-900-S; (c) LSV curves of (1) N-Fe/G(60)-900-S, (2) N-Co/G(60)-900-S, (3) N-Ni/G(60)-900-S and (4) 30% Pt/C; (d) LSV and HO2- yield (e) of (1) N-Fe/G(60)-800-S, (2) N-Fe/G(60)-900-S, (3) N-Fe/G(60)-1000-S and (4) 30% Pt/C; (f) current-time (I-t) responses of N-Fe/NG(60)-900-S and 30% Pt/C at 0.53 V vs. RHE with a rotation rate of 1600 rpm. (Catalyst loading: ~0.500 mg/cm^2 for N-TM/G-S and ~0.125 mg/cm^2 for 30% Pt/C)

Compared in alkaline solution, the excellent catalytic performance in acid solution is more urgently desired, especially for proton exchange membrane fuel cell, but still remains a big challenge currently. To achieve this goal, the prepared catalysts were etched by 2M H_2SO_4 solution at 80°C for 8 hours with subsequent second heat treatment under the same temperature. Excitingly, electrochemical tests in Figure 7 demonstrate that the obtained N-TM/G-S catalysts, especially N-Fe/G-S, have an excellent catalytic performance in 0.1 M $HClO_4$ solution. A typical oxygen reduction peak at 0.631 V vs. RHE appears in the CV curve (Figure 6a) of N-Fe/G (60)-900-S in O_2-satuted 0.1 M $HClO_4$ solution. RDE voltammograms (Figure 6b) of N-Fe/G (60)-900-S reveal that it has a high onset potential of 0.834V (vs. 0.928V of 30% Pt/C), half-wave potential of 0.716V (vs. 0.805V of 30% Pt/C) and diffusion-limiting current density of 5.81 mA/cm^2 (vs. 5.90 mA/cm^2 of 30%Pt/C). The well linear fitting of Koutecky–Levich plots derived from RDE voltammograms at different rotation speed for N-Fe/G (60)-900-S suggests first-order reaction kinetics of ORR on this catalyst. Compared with N-Fe/G (60)-900-S, N-Co/G (60)-900-S and N-Ni/G (60)-900-S catalysts display a weak catalytic activity in acid solution (Figure 6c). Furthermore, the RDE and RRDE test results in Figure 6d-e indicate that a higher treatment temperature than 900^{o}C is necessary for N-Fe/G catalysts to achieve excellent catalytic activity as well as selectivity in acid solution. In addition, the prepared N-Fe/G-S catalyst also displays a better stability and tolerance to methanol crossover effect than that of 30% Pt/C.

In order to reveal the effect on the electrocatalytic performance from the heat treatment temperature, the changes of Fe states in the N-Fe/G catalysts were characterized by Mössbauer spectra. As shown in Figure 7, four doublets are observed in N-Fe (60)-800-S at δ= 0.50 mm/s (ΔE_Q=1.31 mm/s), 0.59 mm/s (2.26 mm/s), 0.89 mm/s (3.59 mm/s) and 1.00 mm/s (2.64 mm/s), assigned to Fe^{II}-N_4/C (D1, LS, 22.6%), Fe^{II}-N_{2+2}/C (D2, IS, 25.4%), N-Fe^{II}-N_{2+2}/C (D3, HS, 19.3%)and Fe^{III}-N_4 (D4, IS, 8.8%), respectively.[40] When the heat treatment temperature is evaluated to 900^{o}C, two doublets are found at δ= 0.31 mm/s (ΔE_Q=0.69 mm/s) and 0.39 mm/s (2.97 mm/s), corresponding to Fe^{II}-N_4/C (D1, IS, 9.8%) and N-Fe^{II}-N_{2+2}/C (D3, HS, 21.7%), respectively.[41] Finally only Fe^{II}-N_4/C at δ= 0.44 mm/s, ΔE_Q=0.87 mm/s (D1, LS, 5.8%) is remained after heat treatment at 1000^{o}C. It has been revealed that among these different states of Fe, Fe^{II}-N_4/C and N-Fe^{II}-N_{2+2}/C have been considered as the effective catalytic activity for ORR in acid solution considering that their empty (for D1 site) or single electron occupied (for D3 site) 3dz^2 orbital can bind oxygen to their Fe^{II} ions in the end-on adsorption mode.[42] Therefore, the excellent catalytic performance should be attributed to the above active sites well-integrated on the highly-opened TM-GC-NG triple junction. However, even though the concentration of these active sites is significantly reduced with the increase of the treatment temperature, it still has an excellent catalytic activity. That should be attributed to the comprehensive action of high graphitic degree, enhanced SSA and the exposure degree of active sites.

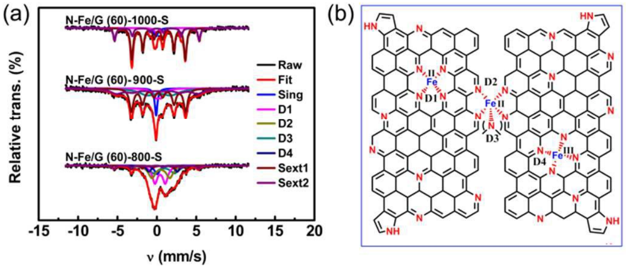

Figure 7. (a) Mössbauer spectra of the catalysts obtained N-Fe/G (60)-T-S and (b) possible structure model of Fe-N bonds. (Sing: Superparam iron; D1: Fe^{II}-N_4/C, low spin (LS); D2: Fe^{II}-N_{2+2}/C, intermediate spin (IS); D3: N-Fe^{II}-N_{2+2}/C, high spin (HS); D4: Fe^{III}-N_4/C; Sext1: Fe_3C; Sext2: α-Fe.)

Based on the above analysis over the composition/structures of the as-prepared catalysts and their electrocatalytic performance, it can be concluded that nitrogen-doped sites can be well cooperated with Fe^{II}-N_4/C sites to effectively catalyse oxygen to hydroxyl in alkaline solution, while only suitable Fe-N configurations (for example, Fe^{II}-N_4/C and N-Fe^{II}-N_{2+2}/C) are more responsible for the catalytically transformation of oxygen to water in acid solution. Such significant difference is probably derived from the diverse catalytic mechanism in different conditions. In addition, based on the confinement effect hypothesis proposed by the group of X. H Bao,[43, 44] we consider that the metal NPs encapsulated by GC shells (mostly above 3 layers) probably cannot participate the ORR, but facilitate the formation of the graphitic structure as well as stable incorporation of nitrogen (especially pydinic and graphitic nitrogen) into them during high-temperature pyrolysis process.[45]

Conclusions

In summary, we have demonstrated a versatile bottom-up protocol towards controllable synthesis of high-performance N-TM/G catalysts with strong-coupled triple junction structure for ORR both in alkaline and acid solution. The extensive controllability on the interfacial structure as well as the states of active sites can be facilely achieved via prompt regulation of the experimental factors. As a result, the optimized N-Fe/G catalyst possesses a superior catalytic activity, selectivity, stability and methanol-resistance ability both in 0.1M KOH and $HClO_4$ solution. It should be attributed to the well-integration of multiple active sites on the highly-opened and strong-coupled TM-GC-NG interfaces via synchronization construction route, leading to an enhanced synergy effect for ORR. Such persistent catalytic performance in alkaline or acid solution with the present of methanol provide a greater probability and feasibility than before for the replacement of Pt-based precious metal catalysts with NPMCs used in different electrochemical energy devices, such as proton exchange membrane fuel cell, direct methanol fuel cell and Zn-air battery.

Acknowledgements

The authors gratefully acknowledge financial support from the National Natural Science Foundation of China (Grant No. 21273114), the Natural Science Foundation of Jiangsu Province (Grant No. BK2012791), the Fundamental Research Funds for the Central Universities (Grant NO. NE2015003) and the “Six Talent Peaks Program” of Jiangsu Province (Grant No. 2013-XNY-010), a Project Funded by the Priority Academic Program Development of Jiangsu Higher Education Institution.

Notes and references

1 A. S. Arico, P. Bruce, B. Scrosati, J. M. Tarascon, W. van Schalkwijk, *Nat. Mater.,* 2005, **4**, 366-377.
2 J. R. Miller, P. Simon, *Science,* 2008, **321**, 651-652.
3 H. A. Gasteiger, N. M. Marković, *Science,* 2009, **324**, 48-49.
4 F. Cheng, J. Chen, *Chem. Soc. Rev.,* 2012, **41**, 2172-2192.
5 J. B. Goodenough, K.-S. Park, *J. Am.Chem. Soc.,* 2013, **135**, 1167-1176.
6 M. K. Debe, *Nature,* 2012, **486**, 43-51.
7 F. Jaouen, E. Proietti, M. Lefevre, R. Chenitz, J. P. Dodelet, G. Wu, H. T. Chung, C. M. Johnston, P. Zelenay, *Energy Environ. Sci.,* 2011, **4**, 114-130.
8 R. Bashyam, P. Zelenay, *Nature,* 2006, **443**, 63-66.
9 S. L. Candelaria, Y. Shao, W. Zhou, X. Li, J. Xiao, J. G. Zhang, Y. Wang, J. Liu, J. Li, G. Cao, *Nano Energy,* 2012, **1**, 195-220.
10 L. Dai, D. W. Chang, J. B. Baek, W. Lu, *Small,* 2012, **8**, 1130-1166.
11 S. Han, D. Wu, S. Li, F. Zhang, X. Feng, *Adv. Mater.,* 2014, **26**, 849-864.
12 D. S. Su, R. Schlögl, *ChemSusChem,* 2010, **3**, 136-168.
13 D. Yu, E. Nagelli, F. Du, L. Dai, *J. Phys. Chem. Lett.,* 2010, **1**, 2165-2173.
14 G. Wu, P. Zelenay, *Acc. Chem. Res.,* 2013, **46**, 1878-1889.
15 D. S. Su, S. Perathoner, G. Centi, *Chem. Rev.,* 2013, **113**, 5782-5816.
16 Q. Li, R. Cao, J. Cho, G. Wu, *Adv. Energy Mater.,* 2014, **4**, 10.1002/aenm.201301415.
17 G. Wu, K. L. More, C. M. Johnston, P. Zelenay, *Science,* 2011, **332**, 443-447.
18 E. Proietti, F. Jaouen, M. Lefèvre, N. Larouche, J. Tian, J. Herranz, J. P. Dodelet, *Nat. Commun.,* 2011, **2**, 416.
19 Y. Zhao, L. Yang, S. Chen, X. Wang, Y. Ma, Q. Wu, Y. Jiang, W. Qian, Z. Hu, *J. Am. Chem. Soc.,* 2013, **135**, 1201-1204.
20 Q. Wang, Z. Y. Zhou, Y. J. Lai, Y. You, J. G. Liu, X. L. Wu, E. Terefe, C. Chen, L. Song, M. Rauf, N. Tian, S. G. Sun, *J. Am. Chem. Soc.,* 2014, **136**, 10882-10885.
21 C. E. Szakacs, M. Lefevre, U. I. Kramm, J.-P. Dodelet, F. Vidal, *Phys. Chem. Chem. Phys.,* 2014, **16**, 13654-13661.
22 Y. Liang, Y. Li, H. Wang, J. Zhou, J. Wang, T. Regier, H. Dai, *Nat. Mater.,* 2011, **10**, 780-786.
23 H. Peng, Z. Mo, S. Liao, H. Liang, L. Yang, F. Luo, H. Song, Y. Zhong, B. Zhang, *Sci. Rep.,* 2013, **3**, 10.1038/srep01765.
24 Y. Hou, T. Huang, Z. Wen, S. Mao, S. Cui, J. Chen, *Adv. Energy Mater.,* 2014, **4**, 1002/aenm. 201400337.
25 H. Wang, H. Dai, *Chem. Soc.Rev.,* 2013, **42**, 3088-3113.
26 Y. Liang, Y. Li, H. Wang, H. Dai, *J. Am. Chem. Soc.,* 2013, **135**, 2013-2036.
27 H. R. Byon, J. Suntivich, Y. Shao-Horn, *Chem. Mater.,* 2011, **23**, 3421-3428.
28 S. Li, D. Wu, C. Cheng, J. Wang, F. Zhang, Y. Su, X. Feng, *Angew. Chem. Int. Ed.,* 2013, **52**, 12105-12109.
29 X. H. Li, S. Kurasch, U. Kaiser, M. Antonietti, *Angew. Chem. Int. Ed.,* 2012, **51**, 9689-9692.

30 T. P. Fellinger, A. Thomas, J. Y. Yuan and M. Antonietti, *Adv. Mater.*, 2013, **25**, 5838-5854
31 X. F. Liu, C. Giordano and M. Antonietti, *Small*, 2014, **10**, 193-200
32 S. Porada, F. Schipper, M. Aslan, M. Antonietti, V. Presser and T. P. Fellinger, *ChemSusChem*, 2015, **8**, 1867-1874.
33 Z. Wen, S. Ci, F. Zhang, X. Feng, S. Cui, S. Mao, S. Luo, Z. He, J. Chen, *Adv. Mater.,* 2012, **24**, 1399-1404.
34 X. B. Zhang, J. M. Yan, S. Han, H. Shioyama, Q. Xu, *J. Am. Chem. Soc.,* 2009, **131**, 2778.
35 K. T. Lee, X. Ji, M. Rault, L. F. Nazar, *Angew. Chem. Int. Ed.,* 2009, **48**, 5661-5665.
36 Y. Zhang, J. Ge, L. Wang, D. Wang, F. Ding, X. Tao, W. Chen, *Sci. Rep.,* 2013, **3**, 10.1038/srep02771.
37 W. Yang, T. P. Fellinger, M. Antonietti, *J. Am. Chem. Soc.,* 2011, **133**, 206-209.
38 L. Lai, J. R. Potts, D. Zhan, L. Wang, C. K. Poh, C. Tang, H. Gong, Z. Shen, J. Lin, R. S. Ruoff, *Energy Environ. Sci.,* 2012, **5**, 7936-7942.
39 M. Ferrandon, A. J. Kropf, D. J. Myers, K. Artyushkova, U. Kramm, P. Bogdanoff, G. Wu, C. M. Johnston, P. Zelenay, *J. Phys. Chem. C,* 2012, **116**, 16001-16013.
40 U. I. Kramm, M. Lefèvre, N. Larouche, D. Schmeisser, J. P. Dodelet, *J. Am. Chem. Soc.,* 2014, **136**, 978-985.
41 U. I. Kramm, J. Herranz, N. Larouche, T. M. Arruda, M. Lefevre, F. Jaouen, P. Bogdanoff, S. Fiechter, I. Abs-Wurmbach, S. Mukerjee, J. P. Dodelet, *Phys. Chem. Chem. Phys.,* 2012, **14**, 11673-11688.
42 Z. L. Wang, D. Xu, H. X. Zhong, J. Wang, F. L. Meng, X. B. Zhang, *Sci. Adv.,* 2015, **1**, e1400035, 10.1126/sciadv.1400035.
43 X. Pan and X. Bao, *Acc. Chem. Res.*, 2011, **44**, 553-562.
44 J. Deng, P. Ren, D. Deng and X. Bao, *Angew. Chem. Int. Ed.*, 2015, **54**, 2100-2104.
45 N. P. Subramanian, X. Li, V. Nallathambi, S. P. Kumaraguru, H. Colon-Mercado, G. Wu, J. W. Lee, B. N. Popov, *J. Power Sources*, 2009, **188**, 38-44.